

# Lawrence Berkeley National Laboratory

## LBL Publications

### Title

Probing the Impact of Radio-mode Feedback on the Properties of the Cool Circumgalactic Medium

### Permalink

<https://escholarship.org/uc/item/4bk3t8r9>

### Journal

The Astrophysical Journal, 974(2)

### ISSN

0004-637X

### Authors

Chang, Yu-Ling

Lan, Ting-Wen

Prochaska, J Xavier

et al.

### Publication Date

2024-10-01

### DOI

10.3847/1538-4357/ad6c44

### Copyright Information

This work is made available under the terms of a Creative Commons Attribution License, available at <https://creativecommons.org/licenses/by/4.0/>

Peer reviewed



# Probing the Impact of Radio-mode Feedback on the Properties of the Cool Circumgalactic Medium

Yu-Ling Chang<sup>1</sup> , Ting-Wen Lan<sup>1,2</sup> , J. Xavier Prochaska<sup>3,4</sup> , Lucas Napolitano<sup>5</sup> , Abhijeet Anand<sup>6</sup> , J. Aguilar<sup>6</sup> , S. Ahlen<sup>7</sup> , D. Brooks<sup>8</sup> , T. Claybaugh<sup>6</sup>, A. de la Macorra<sup>9</sup> , Arjun Dey<sup>10</sup> , P. Doel<sup>8</sup>, S. Gontcho A Gontcho<sup>6</sup> , J. Guy<sup>6</sup> , S. Juneau<sup>10</sup> , T. Kisner<sup>6</sup> , A. Lambert<sup>6</sup>, M. Landriau<sup>6</sup> , L. Le Guillou<sup>11</sup> , M. Manera<sup>12,13</sup> , P. Martini<sup>14,15,16</sup> , A. Meisner<sup>10</sup> , R. Miquel<sup>13,17</sup> , J. Moustakas<sup>18</sup> , A. D. Myers<sup>5</sup>, J. Nie<sup>19</sup> , C. Poppett<sup>6,20,21</sup> , M. Rezaie<sup>22</sup> , G. Rossi<sup>23</sup>, E. Sanchez<sup>24</sup> , M. Schubnell<sup>25,26</sup> , H. Seo<sup>27</sup> , D. Sprayberry<sup>10</sup>, G. Tarlé<sup>26</sup> , B. A. Weaver<sup>10</sup>, and H. Zou<sup>19</sup>

<sup>1</sup> Graduate Institute of Astrophysics, National Taiwan University, No. 1, Sec. 4, Roosevelt Road, Taipei 10617, Taiwan

<sup>2</sup> Department of Physics, National Taiwan University, No. 1, Sec. 4, Roosevelt Road, Taipei 10617, Taiwan

<sup>3</sup> University of California, Santa Cruz, 1156 High Street, Santa Cruz, CA 95064, USA

<sup>4</sup> Kavli Institute for the Physics and Mathematics of the Universe, 5-1-5 Kashiwanoha, Kashiwa, 277-8583, Japan

<sup>5</sup> Department of Physics & Astronomy, University of Wyoming, 1000 East University, Department 3905, Laramie, WY 82071, USA

<sup>6</sup> Lawrence Berkeley National Laboratory, 1 Cyclotron Road, Berkeley, CA 94720, USA

<sup>7</sup> Physics Department, Boston University, 590 Commonwealth Avenue, Boston, MA 02215, USA

<sup>8</sup> Department of Physics & Astronomy, University College London, Gower Street, London, WC1E 6BT, UK

<sup>9</sup> Instituto de Física, Universidad Nacional Autónoma de México, Cd. de México C.P. 04510, Mexico

<sup>10</sup> NSF NOIRLab, 950 North Cherry Avenue, Tucson, AZ 85719, USA

<sup>11</sup> Sorbonne Université, CNRS/IN2P3, Laboratoire de Physique Nucléaire et de Hautes Energies (LPNHE), FR-75005 Paris, France

<sup>12</sup> Departament de Física, Serra Hünter, Universitat Autònoma de Barcelona, 08193 Bellaterra (Barcelona), Spain

<sup>13</sup> Institut de Física d'Altes Energies (IFAE), The Barcelona Institute of Science and Technology, Campus UAB, 08193 Bellaterra Barcelona, Spain

<sup>14</sup> Center for Cosmology and AstroParticle Physics, The Ohio State University, 191 West Woodruff Avenue, Columbus, OH 43210, USA

<sup>15</sup> Department of Astronomy, The Ohio State University, 4055 McPherson Laboratory, 140 West 18th Avenue, Columbus, OH 43210, USA

<sup>16</sup> The Ohio State University, Columbus, OH 43210, USA

<sup>17</sup> Institució Catalana de Recerca i Estudis Avançats, Passeig de Lluís Companys, 23, 08010 Barcelona, Spain

<sup>18</sup> Department of Physics and Astronomy, Siena College, 515 Loudon Road, Loudonville, NY 12211, USA

<sup>19</sup> National Astronomical Observatories, Chinese Academy of Sciences, A20 Datun Road, Chaoyang District, Beijing, 100012, People's Republic of China

<sup>20</sup> Space Sciences Laboratory, University of California, Berkeley, 7 Gauss Way, Berkeley, CA 94720, USA

<sup>21</sup> University of California, Berkeley, 110 Sproul Hall #5800, Berkeley, CA 94720, USA

<sup>22</sup> Department of Physics, Kansas State University, 116 Cardwell Hall, Manhattan, KS 66506, USA

<sup>23</sup> Department of Physics and Astronomy, Sejong University, Seoul, 143-747, Republic of Korea

<sup>24</sup> CIEMAT, Avenida Complutense 40, E-28040 Madrid, Spain

<sup>25</sup> Department of Physics, University of Michigan, Ann Arbor, MI 48109, USA

<sup>26</sup> University of Michigan, Ann Arbor, MI 48109, USA

<sup>27</sup> Department of Physics & Astronomy, Ohio University, Athens, OH 45701, USA

Received 2024 May 13; revised 2024 July 30; accepted 2024 August 5; published 2024 October 11

## Abstract

We explore the influence of radio-mode feedback on the properties of the cool circumgalactic medium (CGM). To this end, we assemble a statistical sample of approximately 30,000 radio galaxies with background quasars by combining optical spectroscopic measurements of luminous red galaxies and quasars from the year 1 data set of the Dark Energy Spectroscopic Instrument and radio sources from the Low-Frequency ARray Two-metre Sky Survey (LoTSS) DR2 catalog and the Very Large Array Sky Survey (VLASS) quick-look catalog. Galaxies with similar optical properties but with no radio counterparts in LoTSS and VLASS are selected as the control group. We measure the cool CGM properties of radio galaxies and their control samples traced by Mg II absorption lines, including covering fraction, rest equivalent width, and gas kinematics. Our results show no significant difference in the properties of gas around radio galaxies and their control sample, indicating that the operating radio-mode feedback of massive galaxies does not produce detectable effects on the properties of the cool CGM. Finally, we show that the CGM of radio galaxies contains a nonnegligible amount of cool gas with approximately  $10^{10} M_{\odot}$ . This abundance can place a stringent constraint on the radio-mode feedback models.

*Unified Astronomy Thesaurus concepts:* [Spectroscopy \(1558\)](#); [Radio active galactic nuclei \(2134\)](#); [Jets \(870\)](#); [Extragalactic astronomy \(506\)](#); [Circumgalactic medium \(1879\)](#)

## 1. Introduction

Feedback from supermassive black holes has been considered as a crucial mechanism driving galaxy evolution (see, e.g., Fabian 2012; Crain & van de Voort 2023 for a review). It is required to be included in simulations in order to explain

salient observed properties of galaxies, especially the massive end of galaxy stellar mass function (e.g., Benson et al. 2003; Bower et al. 2006; Croton et al. 2006; Hirschmann et al. 2014; Beckmann et al. 2017; Kondapally et al. 2023). It is also a key component to reconcile the so-called cooling flow problem (e.g., Cowie & Binney 1977; Fabian & Nulsen 1977), indicating that the gas in massive halos is expected to cool in a short period based on the X-ray emission of hot gas and to condense into new stars—a trend that is not observed. The energy output from the feedback mechanisms has been treated



Original content from this work may be used under the terms of the [Creative Commons Attribution 4.0 licence](#). Any further distribution of this work must maintain attribution to the author(s) and the title of the work, journal citation and DOI.

as the main source to balance this gas cooling (Rafferty et al. 2006; Nulsen et al. 2007; Fabian 2012; Hlavacek-Larrondo et al. 2012; McNamara & Nulsen 2012). In other words, in the current galaxy formation theory, feedback from supermassive black holes regulates the amount of gas in and out of galaxies as well as maintains the thermal content of the circumgalactic medium (CGM; see, e.g., Tumlinson et al. 2017 for a review).

One line of evidence showing the impact of feedback on the CGM properties is from observations of galaxy clusters, such as Perseus and Cygnus A, in X-ray and radio wavelengths (e.g., Boehringer et al. 1993; Carilli et al. 1994; Fabian et al. 2003; McNamara et al. 2005; Bîrzan et al. 2008; Gitti et al. 2012; Pandge et al. 2019; Eckert et al. 2021). These observations demonstrate that hot gas ( $T \sim 10^6$ – $10^7$  K) distribution in these galaxy clusters is clearly affected by the radio jets from supermassive black holes, the so-called radio-mode feedback (see, e.g., McNamara & Nulsen 2012; Heckman & Best 2014; Hardcastle & Croston 2020 for a review). Based on the observations, the estimated required energy to create the cavity of hot gas and the energy output from the radio-mode feedback are consistent with each other. This indicates that radio-mode feedback from supermassive black holes can prevent the cooling of the hot atmosphere, regulate the gas supply, and indeed account for the quenching of massive galaxies. Recent galaxy simulations and subgrid models incorporating radio-mode feedback have successfully reproduced the observed luminosity function of massive galaxies (e.g., Bower et al. 2006; Croton et al. 2006; Gabor et al. 2011; Davé et al. 2012; Zinger et al. 2020).

While the influence of radio-mode feedback on the properties of the CGM has been studied, the observations have mostly focused on (1) massive systems, such as galaxy clusters ( $M_{\text{halo}} > 10^{14} M_{\odot}$ ), and (2) the hot gas ( $T \geq 10^6$  K) properties via X-ray observations (e.g., McNamara & Nulsen 2007). There are limited observational efforts probing relatively less massive halos and the properties of the cool CGM ( $T \sim 10^4$  K), which can also be sensitive to radio-mode feedback and a strong constraint on the corresponding models (Huang et al. 2016; Smailagić et al. 2023).

To probe the cool CGM properties of galaxies with radio-mode feedback in operation, one can utilize absorption line spectroscopy (e.g., Tumlinson et al. 2017), that is, by constructing a sample of galaxies with radio emission having bright sources, such as quasars, in the background with lines of sight (LoSs) intercepting the CGM of the galaxies. However, the number of galaxies with radio emission and with background quasars detectable by wide-field radio surveys is rare. This limits the observational ability to probe the impact of radio-mode feedback on the properties of the cool CGM, and there are only a limited number of relevant studies (e.g., Kauffmann et al. 2017) to date.

In this work, we overcome this observational limitation by utilizing the large optical spectroscopic data set obtained by the Dark Energy Spectroscopic Instrument (DESI) survey (DESI Collaboration et al. 2016a, 2022) and the large source catalogs provided by two radio sky surveys, the LOw-Frequency ARray Two-metre Sky Survey (LoTSS; Shimwell et al. 2017) and the Very Large Array Sky Survey (VLASS; Lacy et al. 2020). Through this approach, we study the properties of the cool CGM around massive galaxies, such as luminous red galaxies (LRGs), with radio-mode feedback in action and compare the gas properties with that of a control sample without radio

emission. This adds a new parameter that has not been extensively explored in previous studies of the properties of gas around LRGs (e.g., Zhu et al. 2014; Huang et al. 2016; Lan & Mo 2018; Anand et al. 2021).

Combining radio emission signals with optical galaxy properties, we construct a sample of radio galaxies with  $z > 0.4$  with background quasars as well as a control sample without radio emission and measure the properties of the cool CGM traced by Mg II absorption lines  $\lambda\lambda 2796, 2803$ , an absorption line species that has been widely used to probe the CGM content across cosmic time (e.g., Lanzetta et al. 1987; Nestor et al. 2005; Nielsen et al. 2013; Zhu & Ménard 2013a; Lan et al. 2014; Huang et al. 2016; Raghunathan et al. 2016; Chen et al. 2017; Lan & Mo 2018; Lan 2020; Anand et al. 2021, 2022; Zou et al. 2021, 2024), and explore the correlation between the gas properties and the presence of radio emission, a proxy of radio-mode feedback in action.

This paper is organized in the following way. Section 2 describes our sample and data, and Section 3 presents how we obtain the properties of the Mg II absorption lines. We show our results in Section 4 and discuss the implications in Section 5. Section 6 summarizes the paper. Throughout the paper, we adopt a flat  $\Lambda$ CDM cosmology with the following parameters:  $\Omega_m = 0.3$  and  $H_0 = 70 \text{ km s}^{-1} \text{ Mpc}^{-1}$ .

## 2. Data

### 2.1. DESI

DESI is mounted on the Mayall 4 m telescope at Kitt Peak National Observatory (DESI Collaboration et al. 2016a, 2016b). It consists of 5000 fibers (Silber et al. 2023) with spectral wavelength coverage ranging from 3600 to 9800 Å and a resolution of 2000–5000 (DESI Collaboration et al. 2022; Guy et al. 2023). The spectroscopic classifications and redshifts for each DESI source are determined using the Redrock pipeline<sup>28</sup> (Brodzeller et al. 2023; Anand et al. 2024). The survey includes dark-time and bright-time observations for different types of sources (Schlafly et al. 2023). The bright-time observations cover stars in our Milky Way (Cooper et al. 2023) and bright galaxies (Hahn et al. 2023; Juneau et al. 2024), while the dark-time observations cover relatively faint extragalactic sources, including LRGs (Zhou et al. 2023), emission line galaxies (Raichoor et al. 2023), and quasars (Chaussidon et al. 2023).

The target selection scheme for the DESI sources (Myers et al. 2023) and the corresponding redshift performance with the DESI observations have been tested and validated during the survey validation (SV) phase, including observations with long exposure times (SV 1) and observations covering about 1% of the whole DESI survey (the One-percent Survey; Alexander et al. 2023; DESI Collaboration et al. 2024a; Lan et al. 2023). In this work, we use the LRG and quasar data from SV (Early Data Release, EDR; DESI Collaboration et al. 2024b) and the first year of the main survey. The cosmological constraints from the baryon acoustic oscillation measurements with the DESI first-year main survey data have been published (DESI Collaboration et al. 2024c, 2024d, 2024e).

*The DESI LRG survey.* LRGs are massive passive galaxies selected based on their colors and brightness with a redshift range  $0.3 < z \leq 1.1$  (Zhou et al. 2023). For our analysis, we

<sup>28</sup> <https://github.com/desihub/redrock>

select LRGs without any warning flag from the DESI pipeline,  $Z_{\text{WARN}} = 0$ ,<sup>29</sup> and with  $\text{DELTA}\chi^2 \Delta\chi^2 > 15$ , a difference of  $\chi^2$  values between the second and first best-fit models, to ensure a robust redshift estimation (Lan et al. 2023; Zhou et al. 2023). We further select LRGs with  $0.4 < z < 1.2$  to ensure that the Mg II absorption lines are within the DESI wavelength coverage. The above selection leads to a sample of  $\sim 2.2 \times 10^6$  LRGs.

*The DESI QSO survey.* The DESI survey observes quasars selected with the random forest algorithm across a wide redshift range from redshift 0.5 to beyond redshift 2 (Chaussidon et al. 2023). Redshift  $> 2.1$  quasars are primarily used as background light for probing the baryonic acoustic oscillation signals via detecting the Ly $\alpha$  forest (e.g., Ramírez-Pérez et al. 2024). Low-redshift quasars can be used as direct tracers of matter distribution. Similarly to the LRG selection, we apply the criteria  $Z_{\text{WARN}} = 0$  and  $\text{DELTA}\chi^2 > 15$  to select DESI QSOs, ensuring that we include only quasars with reliable redshift measurements from the pipeline (Alexander et al. 2023; Chaussidon et al. 2023). We also exclude quasars with a spectral signal-to-noise ratio (S/N) lower than 1, a spectral quality too low to detect absorption lines. Our quasar sample includes  $\sim 1.2 \times 10^6$  sources in total.

## 2.2. Radio Catalogs

*LoTSS.* LoTSS (Shimwell et al. 2017) is an ongoing radio-wavelength (120–168 MHz) sky survey aiming to cover the entire northern sky. The angular resolution is about  $6''$  with sensitivity down to  $\sim 70$ – $100$  mJy. In this work, we make use of the second data release of LoTSS, LoTSS DR2 (Shimwell et al. 2022), which covers approximately 27% of the northern sky with  $\sim 4 \times 10^6$  radio sources. LoTSS DR2 sky coverage overlaps with the sky coverage of the DESI survey in the northern sky, making the DR2 catalog a suitable resource for identifying radio counterparts of the DESI galaxies.

*VLASS quick look.* The Karl G. Jansky VLASS (Lacy et al. 2020) aims to observe the entire northern sky of  $\delta > -40^\circ$  with three epochs at the 2 GHz  $< \nu < 4$  GHz frequency band with  $2''.5$  angular resolution. We use the VLASS data based on the quick-look (QL) imaging (Gordon et al. 2021) from the first two epochs at 3 GHz,<sup>30</sup> including  $\sim 3.5 \times 10^6$  sources. The first two epochs of VLASS QL data exhibit a sensitivity comparable to that of Faint Images of the Radio Sky at Twenty cm,  $\sim 1$  mJy, and cover the entire VLASS footprint.

## 3. Analysis

### 3.1. LRG–QSO Pairs

To study the CGM of radio galaxies, we construct a sample of radio-detected DESI LRGs with background quasars. To this end, we utilize the radio-optical cross-match catalog for the LoTSS DR2 (Hardcastle et al. 2023) and match those optical identifications and DESI LRGs with a  $0''.75$  search radius (Rosario et al. 2020). Additionally, we cross-match the LRGs with radio sources in the VLASS QL catalogs using a  $2''.5$  matching radius. Around 14% and 1.6% of the DESI LRGs have detected radio counterparts in LoTSS and VLASS, respectively. We note that the different detection fractions of LoTSS and VLASS counterparts are due to the sensitivities of

the two surveys.<sup>31</sup> The impact parameter (projected distance,  $r_p$ ) of the galaxies and background quasar sight lines are within 1000 kpc. To avoid potential contamination of radio emissions from background quasars, we only include systems with the distances between quasars and the centers of radio emission being 2 times larger than the distances between LRGs and the centers of radio emission. That is,  $d_{\text{qso}} \geq 2 \times d_{\text{lrq}}$ , where  $d_{\text{lrq}}$  is the angular separation between the LRG and the radio source associated with it and  $d_{\text{qso}}$  is the separation between the QSO and the associated radio source for the foreground LRG.

In order to isolate the effects of radio-mode feedback on the CGM properties of radio galaxies, we create a set of control galaxies for LoTSS pairs and VLASS pairs. For each DESI radio LRG in the LoTSS and VLASS catalogs, two and four control LRGs are respectively selected based on the combined nearest Euclidean distances of four optical properties:  $z$ -band flux, Wide-field Infrared Survey Explorer W1 flux,  $g-r$  color, and redshift.<sup>32</sup> All the control galaxies are required to have no radio detection from LoTSS or VLASS within  $10''$ . For the LoTSS control sample, we select DESI LRGs located in the sky coverage of the LoTSS DR2 footprint without detected radio emission, while for the VLASS control sample, we select DESI LRGs without detected radio emission in the DESI data set given that VLASS covers most of the DESI footprint. For the final control samples, we remove duplicate control systems selected more than one time from different radio-detected LRGs.

Figures 1 and 2 show examples of LRG–QSO pairs and their corresponding radio counterparts for both the experimental groups and the control groups. Figure 3 shows the observed properties of the radio LRGs and the control samples, demonstrating that the two groups have similar optical properties. The main difference is that the control galaxies do not have radio emission detected in the corresponding surveys. We check the radio morphology for the radio-detected LRGs. For the LoTSS-detected sources, we utilize Equation (2) from Shimwell et al. (2022) to identify extended sources. For VLASS-detected sources with peak flux  $> 3$  mJy beam $^{-1}$ , we find the extended source using the deconvoluted-size criteria outlined in Gordon et al. (2021). Our final samples include  $\sim 8\%$  and  $\sim 21\%$  of the extended LRGs for LoTSS and VLASS, consistent with the fraction for all the sources in both radio catalogs.

We also estimate the stellar masses of the LRGs by performing spectral energy distribution fitting with  $g$ ,  $r$ ,  $z$ , and W1 fluxes using CIGALE (Boquien et al. 2019). To model the spectra and obtain the stellar properties with CIGALE, we use a Bruzual & Charlot (2003) model and assume a Chabrier (2003) initial mass function. The stellar mass distributions are shown in Figure 4. The results show that stellar mass distributions between the radio LRGs and their control galaxies are consistent with each other. We note that the VLASS sample has a higher median stellar mass ( $\sim 0.2$  dex) than the LoTSS sample, which is due to the difference of the sensitivity between the two surveys. The VLASS, with its shallower

<sup>31</sup> LoTSS is  $\sim 5$  times deeper than VLASS when converting flux at 3 GHz, assuming  $\alpha = 0.5$ . We have used the radio flux-limited samples (1 mJy for LoTSS and 3 mJy for VLASS) to perform the analyses, which yield consistent results with the whole samples.

<sup>32</sup> Because of the limited number of sources in the LoTSS footprint available for selection as the control group, which is only one-sixth the size of the VLASS control group, adding more control galaxies for each LoTSS LRG would lead to a mismatch in the distribution of optical properties compared to the radio sample.

<sup>29</sup> <https://github.com/desihub/redrock/blob/main/py/redrock/zwarning.py>

<sup>30</sup> <https://cirada.ca/vlasscatalogueq10>

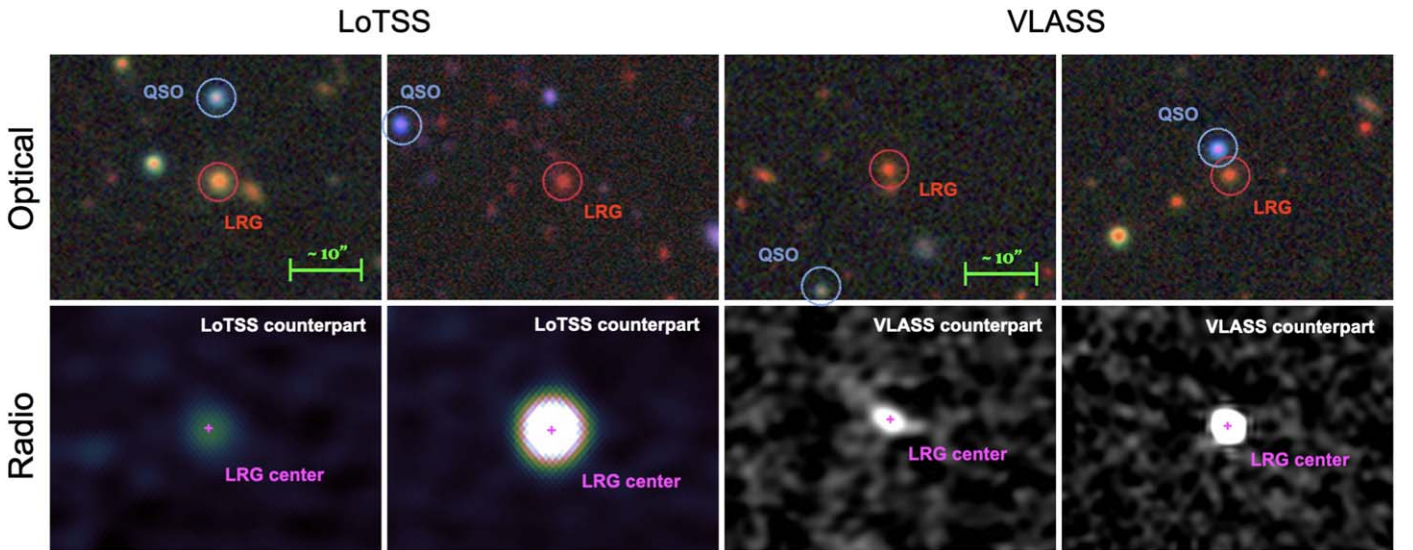


**Figure 1.** Examples of LRG–QSO pairs with radio counterparts in LoTSS (left) and VLASS (right). The upper panels are the optical images from the DESI Legacy Imaging Surveys (Dey et al. 2019), and the lower panels are the radio images from the two radio surveys.

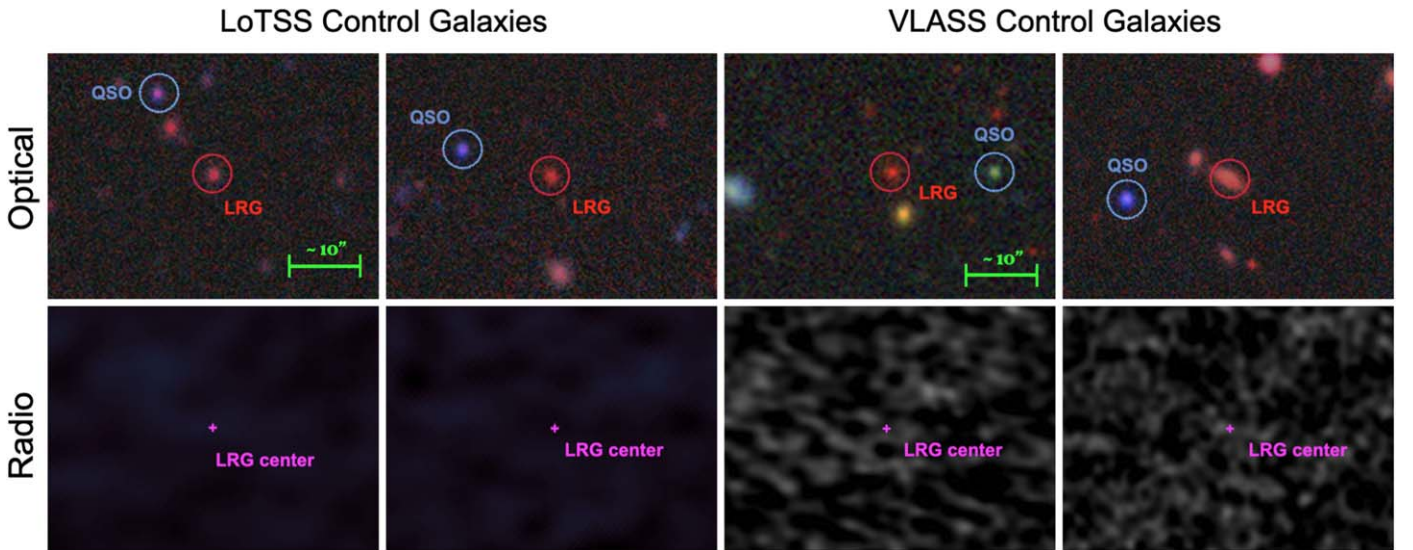


**Figure 2.** Examples of LRG–QSO pairs without radio counterparts in LoTSS (left) and VLASS (right), i.e., the control samples. The upper panels are the optical images from the DESI Legacy Imaging Surveys (Dey et al. 2019), and the lower panels are the radio images from the two radio surveys.

depth, primarily detects brighter radio galaxies, which tend to be more massive (Jarvis & McLure 2002; Best et al. 2005).

We further include the following selections to obtain clean spectral regions for detecting Mg II absorption lines associated with the LRGs.

1. To avoid the possible contamination of QSO-associated absorbers, the velocity difference between LRGs and quasars is required to be  $\delta v \geq 6000 \text{ km s}^{-1}$  (Napolitano et al. 2023).
2. We exclude the spectral regions close to the C IV emission lines of quasars with  $\delta v \lesssim 10,000 \text{ km s}^{-1}$  to avoid broad C IV absorption features.
3. We also exclude pairs with high-redshift quasars with the wavelength region of Mg II absorption lines at the galaxy redshifts overlapping with the Ly $\alpha$  forests with  $\delta v \lesssim 12,000 \text{ km s}^{-1}$ .

Table 1 summarizes the number of pairs after each selection criterion. The final sample consists of 26,949 and 16,013 radio

LRG–quasar pairs from LoTSS and VLASS, respectively, and 37,379 and 59,017 LRG–quasar pairs as the control sample. We note that 9802 pairs overlap between the LoTSS-selected and VLASS-selected samples.

### 3.2. Mg II Absorbers

To detect absorption lines in quasar spectra, the first step is to estimate the continuum intrinsic to the source. We follow the procedure applied in Zhu & Ménard (2013a), utilizing the nonnegative matrix factorization (NMF; Lee & Seung 1999; Zhu 2016) method to estimate the quasar spectral energy distribution with 12 NMF eigenspectrum bases obtained in Zhu & Ménard (2013a). We further apply a median filter with 85 pixels (Napolitano et al. 2023) to remove the small-scale fluctuation on the normalized spectra.

With the normalized quasar spectra, we develop an automatic algorithm to detect Mg II absorption lines around LRGs with the following procedure.

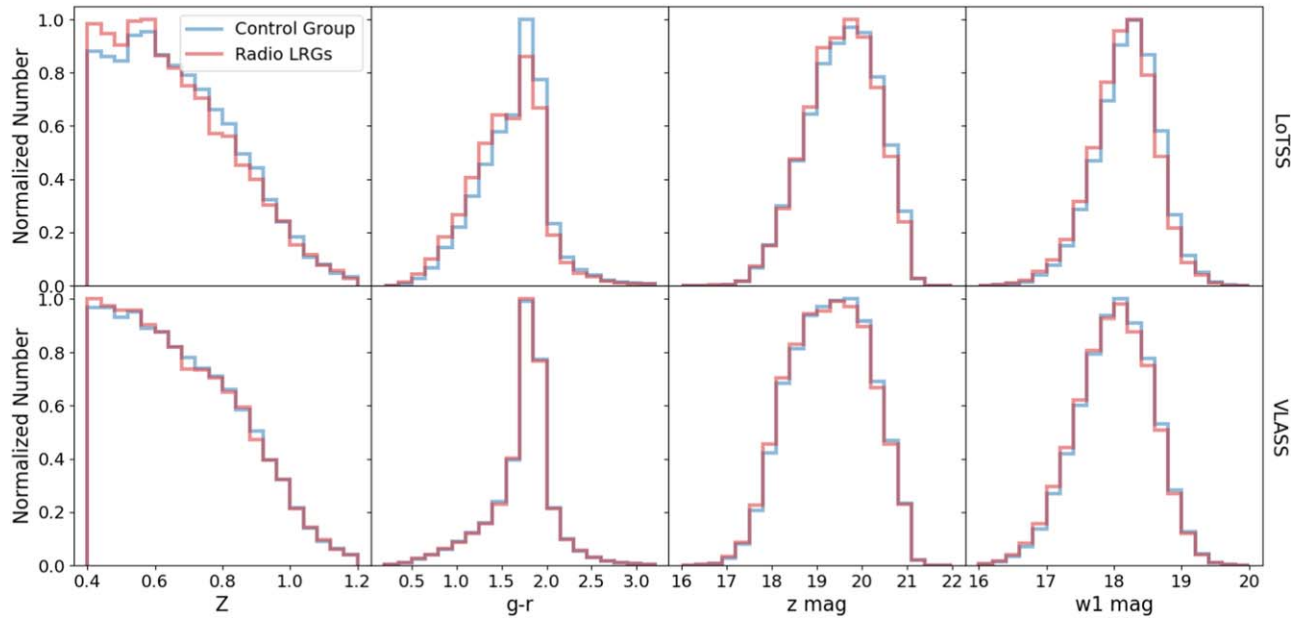


**Figure 3.** Distributions of redshift, color,  $z$ -band magnitude, and W1-band magnitude (from left to right) for the experimental group and the control group from the LoTSS catalog and the VLASS catalog. The upper panels show the properties of the LRGs from the LoTSS samples, while the lower panels show those of the LRGs from VLASS. The red and blue lines represent the radio groups and the control groups, respectively.

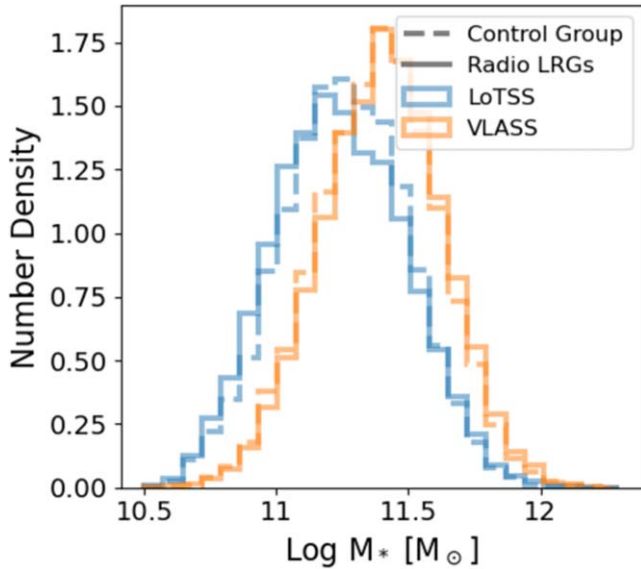


**Figure 4.** Stellar mass distribution of our samples from CIGALE spectral energy distribution fitting. The blue lines show the distribution of the LRGs from the LoTSS samples, while the orange lines show that of the LRGs from the VLASS samples. The dashed and solid lines represent the control groups and radio groups, respectively.

1. We use a matched filter method with a Mg II doublet profile based on Sloan Digital Sky Survey (SDSS) composite spectra (Lan & Fukugita 2017) and convolve the absorption line profile with the pixel values of each normalized spectrum across a velocity window between  $-1000$  and  $1000 \text{ km s}^{-1}$  around the LRG rest frame. We also apply this calculation to the error arrays to estimate the uncertainty of the convolved spectra.
2. From the convolved spectra and the corresponding uncertainty, we identify spectra with pixels having a

<b>Table 1</b>		
Number of Pairs with All the Selection Cuts		
QSO–LRG Pairs within $r_p = 1000 \text{ kpc}$ : 1,279,006		
	LoTSS	VLASS
Select Radio-detected and Control Group		
Radio LRGs	35,720	21,014
Control group	48,923 <sup>a</sup>	77,325 <sup>b</sup>
After Excluding QSO-associated Absorbers		
Radio LRGs	35,197	20,629
Control group	48,165	76,025
After Excluding the Region Close to C IV Emission Lines		
Radio LRGs	31,585	18,601
Control group	43,301	68,343
After Excluding the Region within the Ly $\alpha$ Forest		
Radio LRGs	26,949	16,013
Control group	37,379	59,017

**Notes.**

<sup>a</sup> Two control galaxies with the closest optical properties to each LoTSS-detected LRG are selected. LoTSS covers a much smaller area of the sky compared to VLASS, leading to a limited number of unique control galaxies selected.

<sup>b</sup> Four control galaxies with the closest optical properties to each VLASS-detected LRG are selected.

- maximum signal-to-noise ratio (S/N) greater than 2 and consider the velocity of the pixel with maximum S/N as the central velocity of the Mg II absorber candidate.
3. We use a double Gaussian profile to fit the original normalized spectra at the central velocities of Mg II absorber candidates and measure the absorption line properties, including Mg II rest equivalent widths  $W_{0,\lambda 2796,2803}$ , line widths, and the final best-fit central velocities of the Mg II absorber candidates as well as their corresponding uncertainties.

**Table 2**

The Number of Pairs Used to Detect Mg II Absorption Lines and the Identified Absorbers in Both Experimental and Control Groups from Each Radio Catalog

	Absorbers		LRG–QSO pairs	
	LoTSS	VLASS	LoTSS	VLASS
Radio LRGs	415 1.5%	305 1.9%	26,949 ...	16,013 ...
Control group	542 1.5%	1013 1.7%	37,379 ...	59,017 ...

4. Finally, we consider Mg II absorber candidates with an S/N of  $W_{0,\lambda 2796} \geq 3$  and an S/N of  $W_{0,\lambda 2803} \geq 2$  as detected Mg II absorption lines.

Other absorption line species, such as Fe II and C IV, can accidentally fall within the search window and mimic the Mg II absorption line signals. To remove such possible contamination, we use the Mg II line ratio ( $R = W_{0,\lambda 2796}/W_{0,\lambda 2803}$ ) as the criterion. More specifically, we calculate the line ratio distribution as a function of  $W_{0,\lambda 2796}$ , using the DESI EDR Mg II absorber catalog (Napolitano et al. 2023) as a reference. For a given  $W_{0,\lambda 2796}$ , we remove Mg II absorbers whose line ratio values fall outside the 0.135–99.865 percentile of the  $R$  distribution from the DESI EDR Mg II catalog. This removes approximately 3% of the systems.

Our final LRG Mg II absorber samples include 957 and 1318 absorbers selected from the LoTSS and VLASS catalogs, respectively. Approximately 400 and 300 of these absorbers are associated with radio emissions from LoTSS and VLASS. The numbers are summarized in Table 2.

### 3.3. Completeness of the Sample

The detectability of absorption lines depends on the S/N of the quasar spectra and the strengths of the absorption lines (Zhu & Ménard 2013b; Anand et al. 2021). The incompleteness due to undetected absorption lines affects the estimation of intrinsic properties of Mg II absorbers, including the incidence rate around galaxies. To assess the effect of incompleteness and correct for it, we perform a Monte Carlo simulation by creating mock Mg II absorption lines as a function of  $W_{0,\lambda 2796}$  and the S/N of the spectra. The mock Mg II absorption profiles are based on a set of composite spectra built by stacking Mg II absorption lines detected in the DESI year 1 quasar sample (L. Napolitano et al. 2024, in preparation) with the pipeline developed by Napolitano et al. (2023). In the simulations, we have also taken the DESI spectral resolution at different redshifts into account. Finally, we estimate the detection rate ( $N_{\text{recovered}}/N_{\text{input}}$ ) of Mg II absorbers as a function of absorber redshift,  $W_{0,\lambda 2796}$ , and the S/N of the spectra. The details of the detection rate are shown in the Appendix. The inverse of the detection rate is used as a weight,  $w$ , to correct for the undetected absorbers due to the noise of the spectra.

However, using the weights to recover the nondetection will reach its limitation due to the fact that for spectra with a too-low S/N, one cannot detect any absorbers with  $W_{0,\lambda 2796}$  below the noise level. To avoid reaching such a limitation, we adopt a conservative selection. For  $0.4 \text{ \AA} \leq W_{0,\lambda 2796} < 1 \text{ \AA}$ , we only consider the detection from the normalized spectra with  $S/N \geq 6$ , and for  $W_{0,\lambda 2796} \geq 1 \text{ \AA}$ , we only consider the detection from the normalized spectra with  $S/N \geq 2.5$ . These two threshold values

**Table 3**

Number of Detected Mg II Absorption Lines with Different Spectral S/N Cuts

	S/N Cuts by $W_{0,\lambda 2796}$		All S/N $\geq 6$	
	LoTSS	VLASS	LoTSS	VLASS
Radio pairs	264	215	234	177
Control sample	364	785	322	591

**Note.** The S/N cuts for absorbers with  $0.4 \text{ \AA} \leq W_{0,\lambda 2796} < 1 \text{ \AA}$  and absorbers with  $W_{0,\lambda 2796} \geq 1 \text{ \AA}$  are 6 and 2.5, respectively. Here we also show the number of all detected absorbers with a uniform S/N cut of 6.

are determined based on our simulations showing that with such cuts, using weights to correct for the undetected absorbers is effective. Finally, we summarize our samples with the spectral S/N selections in Table 3. In the following, we define “weak” absorbers as having  $0.4 \text{ \AA} \leq W_{0,\lambda 2796} < 1 \text{ \AA}$  and “strong” absorbers as those with  $W_{0,\lambda 2796} \geq 1 \text{ \AA}$ .

## 4. Results

### 4.1. Mg II Covering Fraction

We first explore the radial distribution of gas traced by Mg II absorption lines around DESI radio LRGs and the control sample. To this end, we measure the Mg II covering fraction,  $f_c$ , indicating the probability of detecting absorbers around galaxies with

$$f_c = \frac{\sum_i^{N_{\text{abs}}} w_i}{N_{\text{quasars}}}, \quad (1)$$

where  $w_i$  is the weight for each detected absorber,  $N_{\text{abs}}$  is the total number of detected absorbers, and  $N_{\text{quasar}}$  is the total number of LRG–QSO pairs for detecting Mg II absorbers.

Figure 5 shows the  $f_c$  as a function of  $r_p$  with two  $W_{\lambda 2796}$  bins for strong ( $W_{0,\lambda 2796} \geq 1 \text{ \AA}$ ) and weak ( $0.4 \text{ \AA} \leq W_{0,\lambda 2796} < 1 \text{ \AA}$ ) absorbers, with the upper and lower panels indicating the results for DESI LRGs with LoTSS and VLASS, respectively. The red and blue data points show the  $f_c$  measurements of radio galaxies and the corresponding control sample, respectively. As shown in Figure 5, the covering fraction of strong and weak absorbers decreases with  $r_p$ , which is consistent with the overall gas distribution traced by Mg II absorbers around galaxies (Lan et al. 2014; Zhu et al. 2014; Huang et al. 2016, 2021; Lan & Mo 2018; Lan 2020; Anand et al. 2021). Moreover, we quantify the possible difference in cumulative distributions of the covering fraction between the radio and the control samples with the Kolmogorov–Smirnov (KS) test in two dimensions (Peacock 1983; Fasano & Franceschini 1987),<sup>33</sup>  $W_{\lambda 2796}$  and  $r_p$ . The  $p$ -values for the weak and strong absorbers for LoTSS are 0.420 and 0.275, respectively. For VLASS, the  $p$ -value is 0.668 for the weak absorbers and 0.985 for the strong absorbers. These results indicate no detectable difference in the  $f_c$  between radio LRGs and the control galaxies for both strong and weak absorbers around radio LRGs and the control sample.

To summarize the gas distribution, we use a power-law function,

$$f_c = A \times \left( \frac{r_p}{100 \text{ kpc}} \right)^\gamma, \quad (2)$$

to describe the  $f_c$  measurements for both  $r_p \leq 400 \text{ kpc}$  (solid lines) and the extended range up to  $r_p \leq 1000 \text{ kpc}$  (dashed

<sup>33</sup> <https://github.com/Gabinou/2DKS>

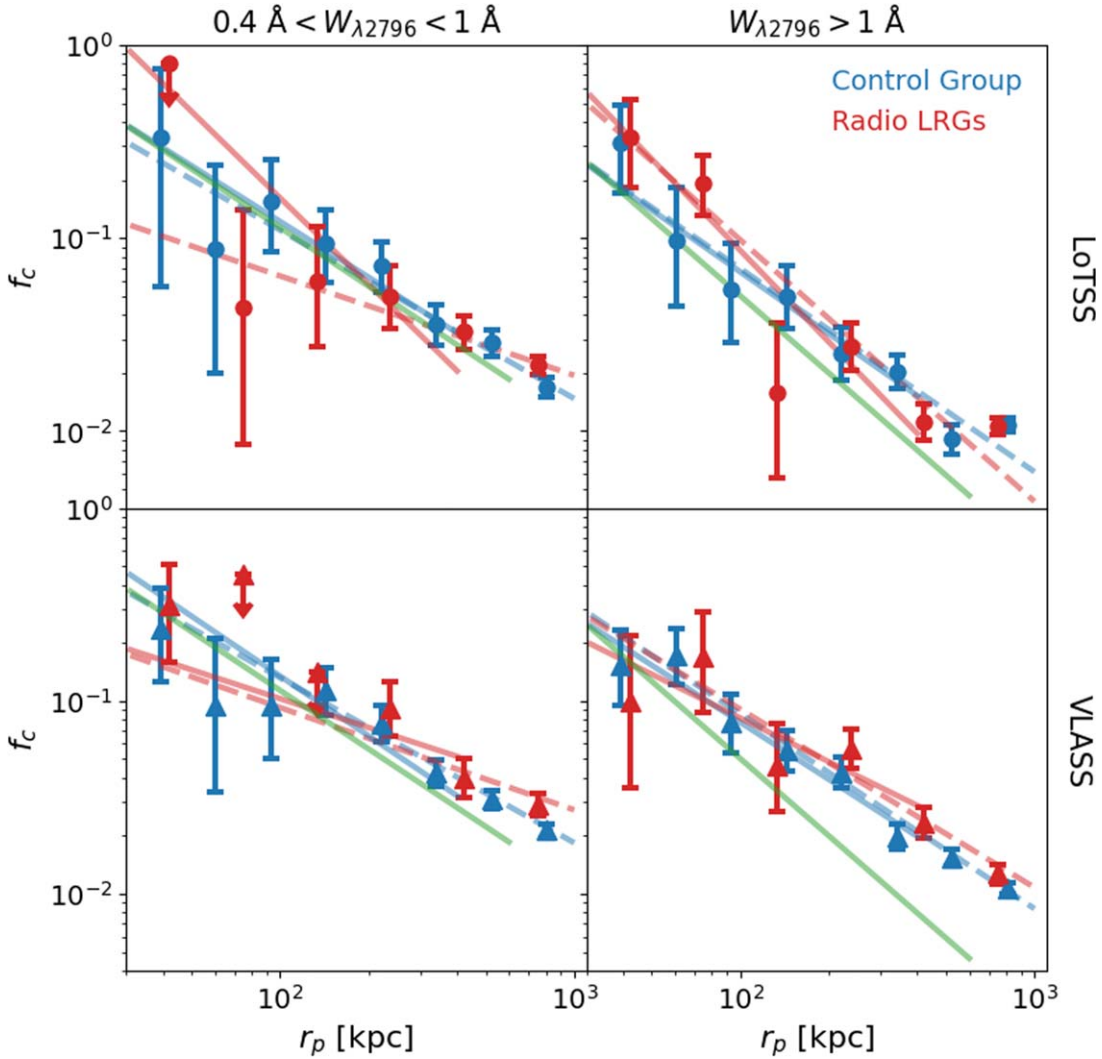


**Figure 5.** Covering fraction ( $f_c$ ) as a function of impact parameter ( $r_p$ ). The upper panels show the  $f_c$  for LRGs from the LoTSS samples, while the lower panels show that for LRGs from the VLASS samples. The  $f_c$  of weak and strong absorbers are depicted correspondingly in the left and right panels. The red and blue points represent the radio groups and control groups, respectively. The errors are estimated based on binomial statistics (Gehrels 1986). Nondetection bins are shown with upper limits, determined at a  $3\sigma$  confidence level. The solid lines and dashed lines illustrate the posterior median of the regression lines for  $r_p \leq 400$  kpc and  $r_p \leq 1000$  kpc. Green lines show the  $f_c$  of passive galaxies in Lan (2020).

lines), as illustrated in Figure 6. To account for the nondetection points (shown as upper limits in the figure), we fit the  $f_c$  with *linmix* (Kelly 2007), sampling the posterior distribution of the regression parameters with the Markov chains. The regression parameters are summarized in Table 4. Figure 6 shows the posterior median of the  $\gamma$ -values of the covering fraction and the  $\gamma$ -values obtained in Lan (2020) within 600 kpc, demonstrating that the measurements within the virial radius of dark matter halos are consistent. The fitting result indicates that the  $f_c$  distribution becomes flatter when considering gas distribution at larger scales  $r_p \leq 1000$  kpc for both weak and strong absorbers. This behavior can be explained by the transition between one-halo and two-halo terms of the matter distribution (e.g., Zhu et al. 2014).

#### 4.2. Rest Equivalent Width Distributions

Besides the covering fraction, we measure the number density distribution of the rest equivalent width,  $W_{0,\lambda 2796}$  ( $dN/dW_{0,\lambda 2796}$ ), around LRGs as shown in Figure 7. Here we

only use systems with quasar spectra  $S/N > 6$  to avoid incompleteness. To focus on absorbers predominantly linked with halos, we display only those within  $r_p \leq 400$  kpc. Following Zhu & Ménard (2013a), we adopt an exponential function,  $dN/dW_{0,\lambda 2796} = N^* \times e^{-W_{0,\lambda 2796}/W^*}$ , to fit the  $W_{0,\lambda 2796}$  number density distribution using *linmix*, and the regression parameters are shown in Table 5. No significant difference is found between the radio LRGs and the control samples for both LoTSS and VLASS, with the KS test  $p$ -values 0.901 and 0.204,<sup>34</sup> respectively. We note that the shape of  $dN/dW_{0,\lambda 2796}$  around LRGs with  $W^* \sim 0.55 \pm 0.05$  is consistent with the shape of the overall Mg II population from Zhu & Ménard (2013a) with  $W^* \simeq 0.6$  at redshift  $\sim 0.65$ .

#### 4.3. Gas Kinematics

We now explore the gas kinematics of radio galaxies by investigating the LoS velocity difference,  $dv$ , between the gas

<sup>34</sup> Here we used a nearly completed sample of sources with  $S/N \geq 8$  for the KS test.



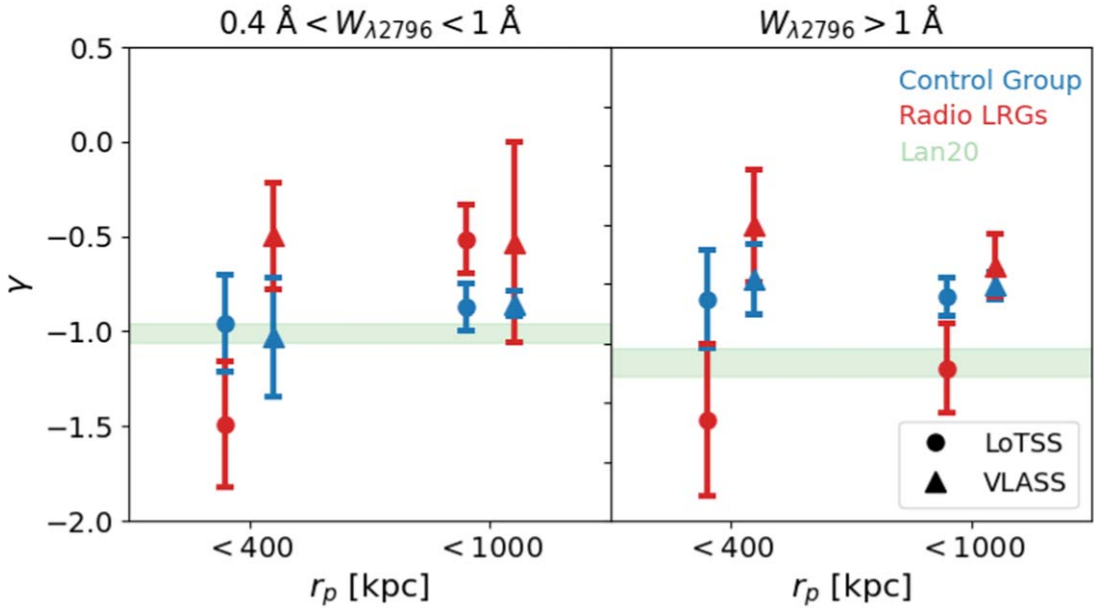


**Figure 6.** The posterior median of the slopes of the regression lines with 68% confidence intervals for covering fraction  $f_c$ . The left and right panels illustrate outcomes specific to weak and strong absorbers. The circles represent LRGs from the LoTSS samples, and the triangles represent those from the VLASS samples. The blue, red, and green data show the results for the control groups, radio groups, and galaxies from Lan (2020), respectively.

**Table 4**

Regression Parameters as Well as 68% Confidence Intervals for Covering Fraction  $f_c$

	$r_p \leq 400$ kpc			
	LoTSS		VLASS	
	$0.4 \text{ \AA} \leq W_{0,\lambda 2796} < 1 \text{ \AA}$			
	$\gamma$	$A$	$\gamma$	$A$
Radio LRGs	$-1.49 \pm 0.33$	$0.16 \pm 0.05$	$-0.50 \pm 0.28$	$0.10 \pm 0.04$
Control group	$-0.96 \pm 0.26$	$0.12 \pm 0.03$	$-1.03 \pm 0.31$	$0.13 \pm 0.03$
	$W_{0,\lambda 2796} \geq 1 \text{ \AA}$			
	$\gamma$	$A$	$\gamma$	$A$
Radio LRGs	$-1.58 \pm 0.32$	$0.09 \pm 0.02$	$-0.75 \pm 0.24$	$0.08 \pm 0.02$
Control group	$-1.07 \pm 0.21$	$0.07 \pm 0.01$	$-0.98 \pm 0.15$	$0.08 \pm 0.01$
	$r_p \leq 1000$ kpc			
	LoTSS		VLASS	
	$0.4 \text{ \AA} \leq W_{0,\lambda 2796} < 1 \text{ \AA}$			
	$\gamma$	$A$	$\gamma$	$A$
Radio LRGs	$-0.52 \pm 0.18$	$0.06 \pm 0.02$	$-0.53 \pm 0.53$	$0.09 \pm 0.17$
Control group	$-0.87 \pm 0.12$	$0.11 \pm 0.03$	$-0.86 \pm 0.06$	$0.13 \pm 0.02$
	$W_{0,\lambda 2796} \geq 1 \text{ \AA}$			
	$\gamma$	$A$	$\gamma$	$A$
Radio LRGs	$-1.36 \pm 0.19$	$0.10 \pm 0.03$	$-0.92 \pm 0.13$	$0.09 \pm 0.02$
Control group	$-1.05 \pm 0.08$	$0.07 \pm 0.01$	$-1.01 \pm 0.06$	$0.09 \pm 0.01$

**Table 5**

Regression Parameters as Well as 68% Confidence Intervals for the Number Density Distribution of  $W_{0,\lambda 2796}$  for Absorbers within  $r_p \leq 400$  kpc

	LoTSS		VLASS	
	$W^*$	$N^*$	$W^*$	$N^*$
Radio LRGs	$0.59 \pm 0.15$	$3.34 \pm 1.21$	$0.45 \pm 0.14$	$5.42 \pm 3.71$
Control group	$0.52 \pm 0.10$	$3.83 \pm 1.60$	$0.55 \pm 0.11$	$3.74 \pm 1.69$

traced by Mg II absorption lines and the galaxies. The  $d\nu$  distributions are shown in Figure 8, where we consider absorbers mostly bounded with the halos within  $r_p \leq 400$  kpc. To quantify the possible difference between the  $d\nu$  distributions, we perform the KS test between the  $d\nu$  distribution of radio LRGs and their control sample. The calculation yields  $p$ -values of 0.507 for the LoTSS sample and 0.061 for the VLASS sample. This indicates that there is no detectable difference in  $d\nu$  distributions between the radio galaxies and control groups from both LoTSS and VLASS. In addition, in Figure 8, we show the  $d\nu$  distribution from SDSS LRGs (Anand et al. 2021). The  $d\nu$  distributions of the LoTSS samples are consistent with the SDSS LRGs, while distributions of the VLASS samples are broader than the distribution of SDSS LRGs. We discuss the difference in Section 5.

We further measure the LoS velocity dispersion as a function of  $r_p$ . For each  $r_p$  bin, we use the median absolute deviation (MAD) scaled to the standard deviation as an estimator for the LoS velocity dispersion and estimate the corresponding errors by bootstrapping. We have subtracted the contribution from the redshift uncertainty of the gas ( $\sim 13 \text{ km s}^{-1}$ ) and the galaxies ( $\sim 40 \text{ km s}^{-1}$ ) in quadrature to measure the intrinsic velocity dispersion of the gas. The redshift uncertainty of the gas is estimated using the mock spectra based on the typical values of the  $W_{0,\lambda 2796}$  line width, background spectrum S/N, and rest-frame spectral bin of our detected absorbers, while the uncertainty of the LRG redshift measurement is taken from

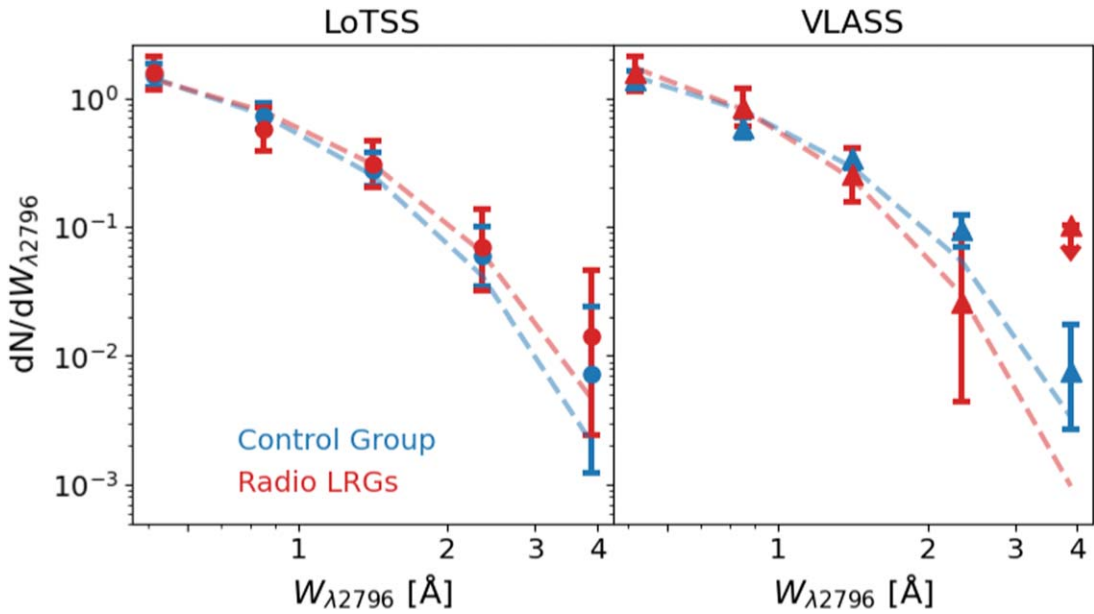


**Figure 7.** Number density distribution of the rest equivalent widths  $W_{0,\lambda 2796}$  for absorbers with  $r_p \leq 400$  kpc. The left and right panels show the distributions respectively corresponding to the absorbers of LRGs from the LoTSS samples and the VLASS samples. The red and blue colors represent the radio groups and the control groups, respectively. The dashed lines are the posterior median of the regression exponential functions. Errors are the confidence levels derived from Poisson statistics (Gehrels 1986).

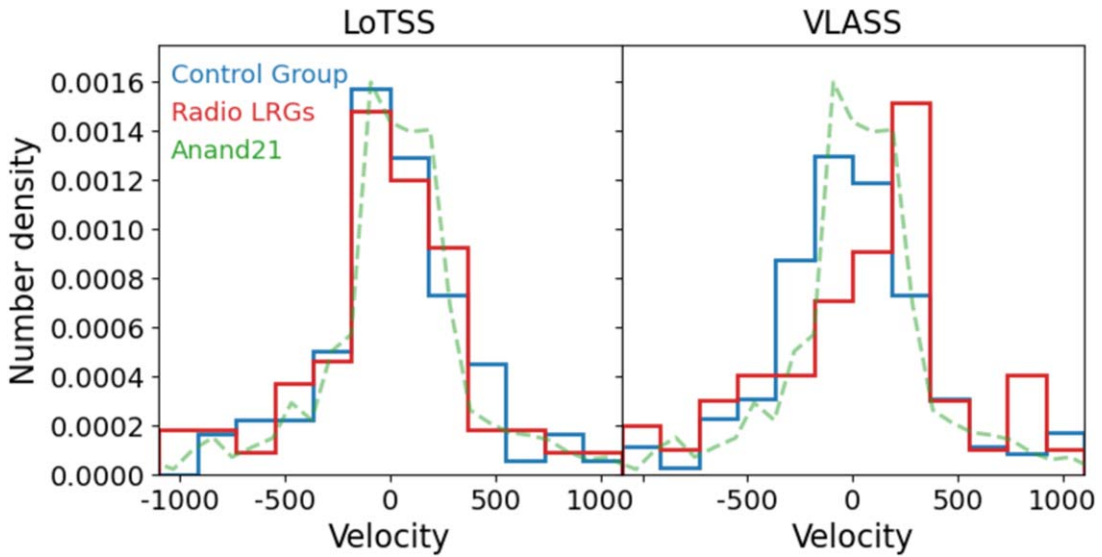


**Figure 8.** Distribution of the LoS gas-galaxy velocity difference ( $dv$ ) of the LRG within  $r_p \leq 400$  kpc. The left panel displays the  $dv$  distribution of LRGs from the LoTSS samples, and the right panel shows that of LRGs from the VLASS samples. The red and blue lines correspondingly represent the radio groups and control groups. We also show the distribution of passive galaxies in Anand et al. (2021).

Lan et al. (2023). The results are illustrated in Figure 9, and Table 6 further shows the dispersion values for sources within  $r_p \leq 400$  kpc and  $r_p > 400$  kpc. We find that the measurements around radio LRGs and the control samples are consistent with each other. For the gas in the inner region ( $r_p \leq 400$  kpc), the radio LRGs and the control samples from both LoTSS and VLASS have a lower velocity dispersion ( $\sigma \sim 200\text{--}300$  km s $^{-1}$ ), similar to the results in previous studies (Zhu et al. 2014; Lan & Mo 2018), while at larger scales, gas exhibits a higher velocity dispersion, reaching  $\sim 500$  km s $^{-1}$ . This behavior is consistent with the contribution from Hubble flow at larger scales.

## 5. Discussion

### 5.1. Comparison with Previous Studies

We compare our measurement of the  $f_c$  ( $W_{0,\lambda 2796} > 0.4$  Å) of radio-detected LRGs with the measurements of SDSS LRGs from Lan & Mo (2018) and Anand et al. (2021) in Figure 10. Overall, the decreasing trends of  $f_c$  are consistent with each other with similar slopes. As DESI and SDSS adopt different criteria for selecting LRG samples, which yield different stellar mass and redshift distributions, we scale the SDSS measurement using the evolution trend based on Lan (2020). If we consider the median redshifts of SDSS LRGs ( $z \sim 0.5$ ) and

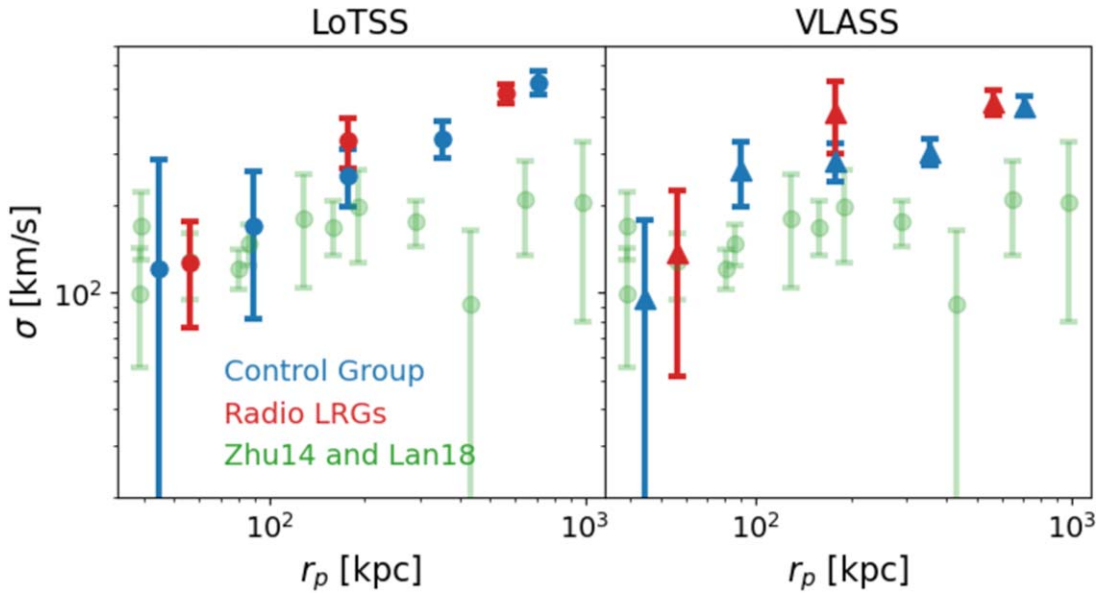


**Figure 9.** Gas velocity dispersion as a function of impact parameter. The left and right panels show the results of LoTSS and VLASS LRGs, respectively. The red, blue, and green points represent the radio LRGs, control groups, and passive galaxies from Zhu et al. (2014) and Lan & Mo (2018), respectively. The velocity dispersion obtained in this work is estimated using MAD scaled to the standard deviation.

**Table 6**

Gas Velocity Dispersion of Our Samples Separated with Two Impact Parameter Bins

	$r_p \leq 400$ kpc		$r_p > 400$ kpc	
	LoTSS ( $\text{km s}^{-1}$ )	VLASS ( $\text{km s}^{-1}$ )	LoTSS ( $\text{km s}^{-1}$ )	VLASS ( $\text{km s}^{-1}$ )
Radio LRGs	$293 \pm 58$	$317 \pm 72$	$483 \pm 38$	$448 \pm 45$
Control group	$236 \pm 42$	$283 \pm 27$	$497 \pm 47$	$429 \pm 30$

radio-detected LRGs ( $z \sim 0.7$ ) in this work, the redshift evolution of the  $f_c$  of strong absorbers will yield  $\left(\frac{1+0.7}{1+0.5}\right)^{2.5} \sim 1.4$ . As illustrated in Figure 10, after adjusting for evolution, the  $f_c$  of the SDSS LRGs from Lan & Mo (2018) and Anand et al. (2021) is consistent with that of the radio-detected LRGs from DESI at a given impact parameter.

In addition to the covering fraction, we observe a larger gas velocity dispersion at larger scales, as compared to the measurement from Zhu et al. (2014; Figure 9). This difference is possibly due to the approaches used to calculate the velocity dispersion. Zhu et al. (2014) measure the velocity dispersion from the composite spectra via stacking analysis. Together with median filtering for spectral processing, this method might mediate the signal far from the line center. We note that, using a similar approach as adopted in this work, Anand et al. (2021) also find a larger velocity dispersion for the gas of LRGs in the outer region.

Finally, among our own measurements, we quantify the potential differences between all the radio and control LRGs selected with LoTSS and VLASS, regardless of whether they have radio emission or not. The gas velocity dispersion<sup>35</sup> of LRGs in the inner CGM ( $< 200$  kpc) for the LoTSS samples is  $216 \pm 32 \text{ km s}^{-1}$ , while that for the VLASS samples is  $306 \pm 38 \text{ km s}^{-1}$ , as illustrated by the blue and orange bands in

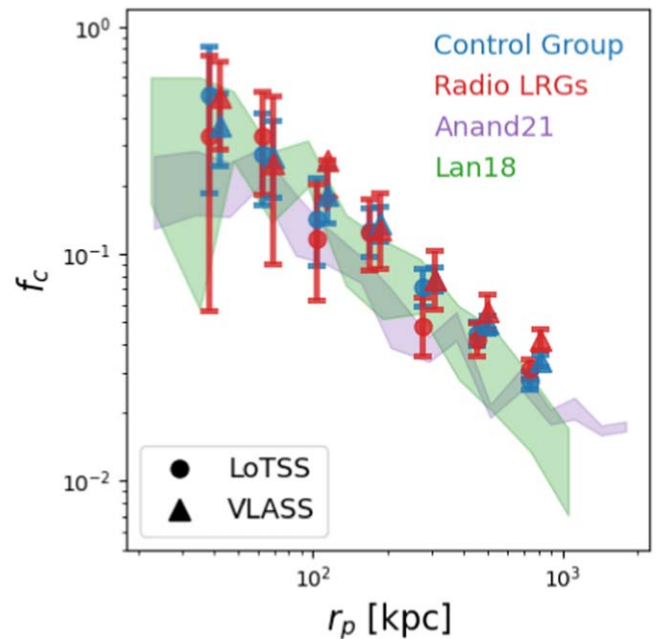


**Figure 10.** Comparison of the covering fraction ( $W_{0.42796} > 0.4 \text{ \AA}$ ) with previous studies. The blue points, orange points, purple band, and green band are the  $f_c$  for the LRGs from our LoTSS samples, our VLASS samples, Anand et al. (2021), and Lan & Mo (2018), respectively. The data from Lan & Mo (2018) and Anand et al. (2021) are scaled to an equivalent redshift of 0.7 using the evolution trend from Lan (2020).

Figure 11. The inner gas around radio-detected LRGs and control LRGs from VLASS exhibits a higher velocity dispersion compared to those from LoTSS. This difference in gas properties can be explained by the stellar mass difference of the two samples. In Figure 11, we divide the sample based on their median stellar mass,  $\sim 10^{11.2} M_\odot$  and  $\sim 10^{11.4} M_\odot$  for LoTSS and VLASS, into high-mass and low-mass sources. The figure indicates that the gas dispersion for the absorbers around high-mass LRGs (stellar mass above the median value) from

<sup>35</sup> Similar to Figure 9, the dispersion shown in this section is estimated using MAD scaled to the standard deviation.

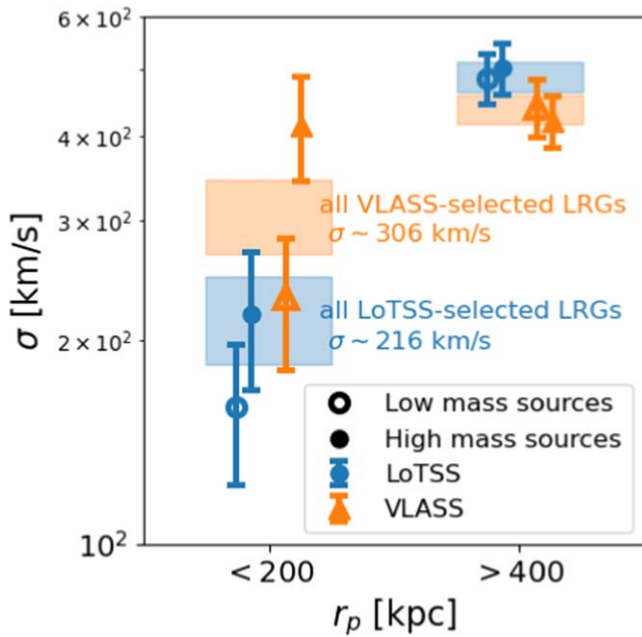


**Figure 11.** Velocity dispersion as a function of stellar masses. The blue data represent both the radio LRGs and the corresponding control galaxies from the LoTSS catalog, while the orange data represent that from the VLASS catalog. The blue and orange bands show the dispersion for all sources selected with LoTSS and VLASS. The filled points are the results from high-mass sources, while the open points are those from low-mass sources. The terms “low-mass sources” and “high-mass sources” refer to those with stellar masses above and below the median of the samples, which is  $10^{11.2} M_{\odot}$  for LoTSS and  $10^{11.4} M_{\odot}$  for VLASS.

VLASS-selected samples is apparently higher than the others. Additionally, LRGs with comparable stellar masses ( $\sim 10^{11} - 10^{11.4}$ ), for LoTSS-selected sources and low-mass VLASS-selected sources, display similar gas dispersion in their CGM. We note that the absorbers beyond  $r_p = 400$  are affected by the halos of other nearby galaxies, and their velocity dispersion is not strongly correlated with the stellar mass.

As shown in Figure 4, the median stellar mass of the VLASS samples is  $\sim 0.2$  dex higher than that of the LoTSS samples. This 0.2 dex difference in the median stellar mass yields a larger difference in halo mass at the high-mass end. Based on the stellar-to-halo mass relation from Girelli et al. (2020), the estimated halo mass difference between the two samples can reach  $\sim 0.5$  dex. If we assume that the typical halo mass of the LoTSS sample is similar to the overall DESI LRG population,  $10^{13.4} M_{\odot}$  (e.g., Yuan et al. 2024), the typical halo mass of the VLASS sample will be about  $10^{13.9} M_{\odot}$ . Their corresponding dark matter velocity dispersion values are  $\sim 270$  and  $\sim 400 \text{ km s}^{-1}$  based on Elahi et al. (2018). This yields a similar subvirial gas motion  $\frac{\sigma_{\text{gas}}}{\sigma_{\text{DM}}} \sim 0.75$  within 200 kpc around the VLASS and LoTSS samples. We note that this value is higher than previous measurements around SDSS LRGs ( $\frac{\sigma_{\text{gas}}}{\sigma_{\text{DM}}} \sim 0.5$ ). We will explore such a difference in the future with the entire DESI LRG sample. The differences in gas kinematics illustrated in Figure 8 between LoTSS-selected and VLASS-selected sources could also be influenced by the disparities in the stellar masses of the two samples. Additionally, the properties of the VLASS samples are consistent with the measurements of galaxy clusters, showing that the CGM in clusters traced by Mg II has a higher covering fraction and

velocity dispersion (e.g., Anand et al. 2022; Cherrey et al. 2024).

### 5.2. CGM Mass around Radio Galaxies

With the covering fraction obtained in Section 4.1, we can quantify the typical amount of cool H I gas around the radio-detected LRGs. We estimate the mass of neutral hydrogen traced by Mg II absorbers residing in the CGM with

$$M_{\text{HI}}(< 400 \text{ kpc}) \sim 2\pi m_{\text{H}} \int_{10 \text{ kpc}}^{400 \text{ kpc}} \hat{N}_{\text{HI}} f_c(r_p) r_p dr_p, \quad (3)$$

where  $\hat{N}_{\text{HI}}$  is the empirical relation between  $W_{0,\lambda 2796}$  and  $N_{\text{HI}}$  from Lan & Fukugita (2017),

$$\hat{N}_{\text{HI}} = 10^{18.96} \left( \frac{W_{0,\lambda 2796}}{1 \text{ \AA}} \right)^{1.69} (1+z)^{1.88} \text{ cm}^{-2}. \quad (4)$$

The median value of the samples  $z \sim 0.67$  is adopted. For weak absorbers, we take the median value of our Mg II absorbers  $W_{0,\lambda 2796} \sim 0.65 \text{ \AA}$ , and for strong absorbers, we take the median value  $W_{0,\lambda 2796} \sim 1.5 \text{ \AA}$ . The final estimated  $M_{\text{HI}}$  for LRGs with LoTSS is  $9.9 \times 10^9 M_{\odot}$  and for LRGs with VLASS is  $1.3 \times 10^{10} M_{\odot}$ . Given that the covering fractions around the control samples are consistent with the radio LRGs, the control samples have a similar mass of neutral hydrogen within 400 kpc. The excess of gas may originate from thermal instabilities in the halos of LRGs (Huang et al. 2016; Nelson et al. 2020), star-forming satellite galaxies within the LRG halos and their neighboring halos (Hafen et al. 2019; Lan 2020), as well as gas accreting through filaments (Kereš et al. 2009; Huang et al. 2016).

This result indicates that there is a nonnegligible amount of cool neutral gas around massive galaxies with possible radio-mode feedback in action. This mass measurement can place constraints on the models of feedback in simulations. For example, Khrykin et al. (2024) use the SIMBA simulations (Davé et al. 2019) to explore the impact of various feedback models on the CGM properties and find that including radio-mode feedback reduces the number of baryons in the CGM by a factor of 5 in halo mass  $\sim 10^{13} M_{\odot}$ , while only reducing it by a factor of 2 as the halo mass increases to  $\sim 10^{13.5} M_{\odot}$ . For another example, Zinger et al. (2020) show that radio-mode feedback changes the thermal properties of the CGM by enhancing the entropy and thereby increasing the gas cooling time. The properties of the cool gas are expected to be affected as well. As summarized in Crain & van de Voort (2023), adopting different assumptions and subgrid recipes of active galactic nucleus (AGN) feedback, the state-of-the-art simulations predict different numbers of baryons in the halos. From these simulations, one can estimate the amount of cool neutral gas around radio galaxies, compare with the measurements reported in this work, and test those feedback models. Furthermore, our gas dispersion measurements could also constrain the gas outflow and their initial velocity for the feedback models (Lan & Mo 2019; Nelson et al. 2019; Mitchell et al. 2020).

### 5.3. Impact of the Radio Jets

From the X-ray and radio observations showing the interaction between radio jets and hot gas, it is expected that radio jets impact the surrounding medium as they propagate.

However, our results show no discernible differences between the properties of the cool CGM of galaxies with and without radio emission. One possibility is that the radio jets do not affect the physical mechanisms producing cool gas around massive galaxies. Apart from this possibility, we discuss three possible scenarios for our results in the following.

*Time and distance scales.* The majority of our radio sources do not have an extended radio emission structure. It is possible that the radio-mode feedback just starts its operation. Therefore, the radio jets do not have sufficient time to propagate into larger scales ( $\sim 100$  kpc; e.g., Hardcastle et al. 2019). To comprehensively analyze gas properties for galaxies with various radio morphologies, more extensive radio surveys are required. These surveys should feature resolution and sensitivity sufficient to distinguish small extended structures and detect low surface brightness sources. Another possibility is that the power of feedback and/or the duration of feedback is not strong and long enough to propagate into larger scales. For radio galaxies with stellar masses around or above  $10^{11} M_{\odot}$ , their typical active period spans 10–100 Myr (e.g., McNamara & Nulsen 2012; Turner & Shabala 2015), and their jets can, on average, span tens of kpc, with the rare bright ones possibly extending to  $\sim 200$ – $300$  kpc or even larger (e.g., Turner & Shabala 2015; Hardcastle et al. 2019; Lan & Prochaska 2021). Given that we only have a handful of sight lines probing the inner CGM, the effect of radio-mode feedback from these bright galaxies might be below the noise level of the current measurements.

*Opening angle.* While powerful radio jets can extend to several hundred kpc, the typical observed jet structures are asymmetric with a certain direction (e.g., Hardcastle & Croston 2020), being consistent with the unified model of AGNs (Urry & Padovani 1995; Netzer 2015; Padovani et al. 2017). For example, based on the observations from the Monitoring Of Jets in Active galactic nuclei with VLBA Experiments program,<sup>36</sup> the radio jets typically have relatively small opening angles with a median value of around  $20^{\circ}$  (Pushkarev et al. 2017). Given the small opening angles, the background LoSs may not intercept the most affected regions by the radio jets. This will dilute the signals and prevent us from detecting the impact of radio jets with a limited number of sight lines in the inner CGM.

*Duty cycle.* Our radio and control samples may come from the same parent population; that is, the gas surrounding the control galaxies can already be influenced by radio jets that stopped recently. Although jets are meant to counteract cooling temporarily, this short lifespan of AGNs ( $\approx$  tens of Myr; Turner & Shabala 2015) is expected to lead to a resumption of the cooling flow (e.g., McNamara & Nulsen 2012), which fuels the central region and triggers the jets once again (e.g., Voit et al. 2020). In other words, AGN activities are expected to occur frequently enough to prevent excessive cooling, with the effects expected to be cumulative (e.g., Donahue & Voit 2022). This hints at the possibility that the CGM, whose host galaxies currently lack radio emission, has previously undergone radio jet activities. Therefore, it is possible that most of our absorbers can be influenced by either current or past radio jets.

DESI is going to observe  $\sim 8$  million LRGs (Zhou et al. 2023) and  $\sim 3$  million QSOs (Chaussidon et al. 2023) during its 5 yr mission. In the first year of the main survey, DESI has

already observed  $\sim 3.5$  million LRGs and  $\sim 1.5$  million QSOs. It is anticipated that the number of known LRG–QSO pairs will triple after DESI completes its operation, with the number of their radio counterparts also expected to increase by approximately threefold. With such a large number of LRG–QSO pairs, we will be able to conduct a more comprehensive study of the relationship between radio jets and the CGM of LRGs.

## 6. Conclusions

We investigate how radio-mode feedback impacts the properties of the cool CGM traced by Mg II absorbers. To this end, we constructed two large samples of  $\sim 30,000$  radio LRGs and background QSO pairs using the latest DESI spectroscopic measurements and two large radio source catalogs from LoTSS and VLASS. We also built two corresponding control galaxy samples that match the host galaxy properties of the radio LRGs but without detected radio emission. With these data sets, we measured and compared the CGM properties around radio LRGs and their control samples and explored possible signals correlating with the presence of radio emission.

Our results show no significant differences between the properties of the cool CGM of radio LRGs and their control samples, including the gas radial distribution, Mg II rest equivalent width distributions, and gas kinematics. This result indicates that there is no detectable correlation between the presence of radio emission and the cool CGM properties. Among the LRG samples, we find that the gas velocity dispersion around radio LRGs in VLASS is higher than that around radio LRGs in LoTSS. This can be explained by the fact that radio LRGs in VLASS on average have higher stellar masses and therefore prefer to live in more massive halos. Finally, we estimate the amount of cool gas mass in the CGM of radio LRGs as being approximately  $10^{10} M_{\odot}$ —a nonnegligible amount of cool gas reservoir. These novel measurements can be used as strong observational constraints on the models of AGN feedback adopted in simulations, providing valuable insights into the impact of radio-mode feedback on baryon distribution around galaxies and the growth of massive galaxies.

In the near future, combining the updated versions of the LoTSS and VLASS catalogs, as well as upcoming deeper and wider sky surveys from the Square Kilometre Array (Braun et al. 2015) and the next-generation VLA (Di Francesco et al. 2019), with optically large spectroscopic data sets, including the complete 5 yr DESI data set, we will be able to increase the sample size by at least a factor of 2 and obtain more precise measurements of the CGM properties of radio galaxies. With such measurements, one will possibly reveal the signatures of radio-mode feedback on the cool CGM for the first time and thereby test the current models of AGN feedback and galaxy evolution.

## Acknowledgments

We thank Vicky Fawcett and Siwei Zou for their constructive comments that greatly helped improve the paper. Y.L.C. and T.W.L. were supported by the National Science and Technology Council (MOST 111-2112-M-002-015-MY3), the Ministry of Education, Taiwan (MOE Yushan Young Scholar grant NTU-110VV007, NTU-111V1007-2, NTU-112V1007-3), and National Taiwan University research grants (NTU-CC-

<sup>36</sup> <https://www.cv.nrao.edu/MOJAVE/index.html>

111L894806, NTU-CC-112L893606, NTU-CC-113L891806). Y.L.C. is supported by NSTC 112-2811-M-002-059.

This material is based upon work supported by the U.S. Department of Energy (DOE), Office of Science, Office of High-Energy Physics, under contract No. DE-AC02-05CH11231 and by the National Energy Research Scientific Computing Center, a DOE Office of Science User Facility under the same contract. Additional support for DESI was provided by the U.S. National Science Foundation (NSF), Division of Astronomical Sciences, under contract No. AST-0950945 to the NSF's National Optical-Infrared Astronomy Research Laboratory; the Science and Technology Facilities Council of the United Kingdom; the Gordon and Betty Moore Foundation; the Heising-Simons Foundation; the French Alternative Energies and Atomic Energy Commission (CEA); the National Council of Science and Technology of Mexico (CONACYT); the Ministry of Science and Innovation of Spain (MICINN); and the DESI Member Institutions: <https://www.desi.lbl.gov/collaborating-institutions>. Any opinions, findings, and conclusions or recommendations expressed in this material are those of the author(s) and do not necessarily reflect the views of the U.S. National Science Foundation, the U.S. Department of Energy, or any of the listed funding agencies.

The authors are honored to be permitted to conduct scientific research on Iolkam Du'ag (Kitt Peak), a mountain with particular significance to the Tohono O'odham Nation.

LOFAR data products were provided by the LOFAR Surveys Key Science project (LSKSP; <https://lofar-surveys.org/>) and were derived from observations with the International LOFAR Telescope (ILT). LOFAR (van Haarlem et al. 2013) is the Low

Frequency Array designed and constructed by ASTRON. It has observing, data processing, and data storage facilities in several countries that are owned by various parties (each with their own funding sources) and collectively operated by the ILT foundation under a joint scientific policy. The efforts of the LSKSP have benefited from funding from the European Research Council, NOVA, NWO, CNRS-INSU, the SURF Co-operative, the UK Science and Technology Funding Council, and the Jülich Supercomputing Centre.

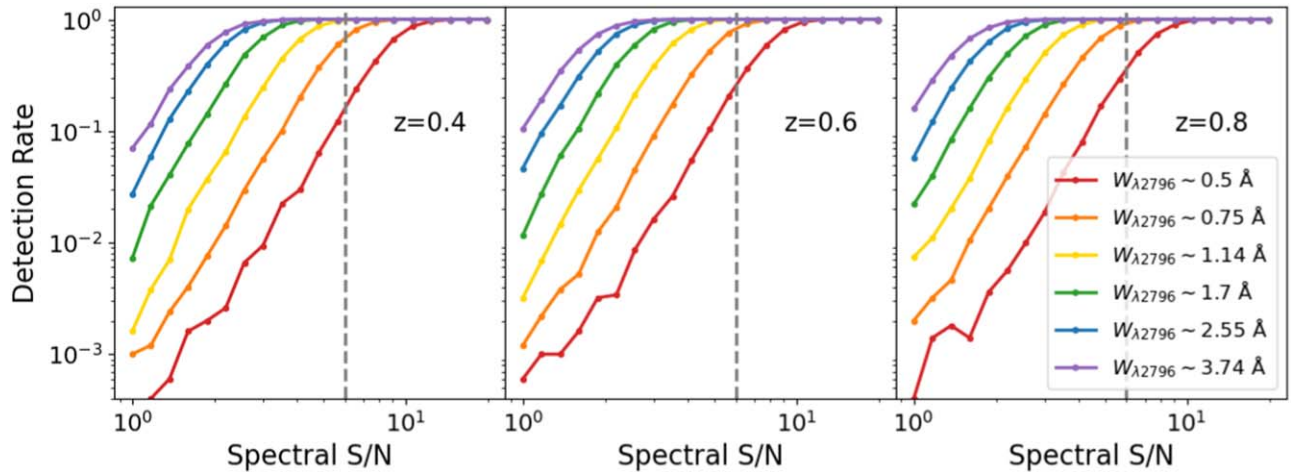
The National Radio Astronomy Observatory is a facility of the National Science Foundation operated under cooperative agreement by Associated Universities, Inc. CIRADA is funded by a grant from the Canada Foundation for Innovation 2017 Innovation Fund (Project 35999), as well as by the Provinces of Ontario, British Columbia, Alberta, Manitoba, and Quebec.

### Data Availability

All data points shown in the figures are available in machine-readable form on Zenodo doi:[10.5281/zenodo.11143902](https://doi.org/10.5281/zenodo.11143902).



### Appendix Detection Rate Simulation

We simulated the detection rate using mock absorption lines to calibrate the number of detected weak absorbers found in realistic QSO spectra with low S/N. Figure 12 illustrates the detection rate of Mg II absorbers as a function of absorber redshift,  $W_{0,\lambda 2796}$ , and the S/N of the spectra. More details about the completeness of our absorption samples are shown in Section 3.3.



**Figure 12.** Detection rate of Mg II absorbers as a function of absorber redshift,  $W_{0,\lambda 2796}$ , and the S/N of the spectra. The left to right panels show the results for redshift bins 0.4, 0.6, and 0.8, respectively. The different colors represent various rest equivalent widths for the mock spectra. The vertical dashed lines represent the spectral S/N cut ( $S/N = 6$ ) for weak absorbers ( $0.4 \text{ \AA} < W_{0,\lambda 2796} < 1 \text{ \AA}$ ).

## ORCID iDs

Yu-Ling Chang  <https://orcid.org/0000-0002-0196-3496>  
 Ting-Wen Lan  <https://orcid.org/0000-0001-8857-7020>  
 J. Xavier Prochaska  <https://orcid.org/0000-0002-7738-6875>  
 Lucas Napolitano  <https://orcid.org/0000-0002-5166-8671>  
 Abhijeet Anand  <https://orcid.org/0000-0003-2923-1585>  
 J. Aguilar  <https://orcid.org/0000-0003-0822-452X>  
 S. Ahlen  <https://orcid.org/0000-0001-6098-7247>  
 D. Brooks  <https://orcid.org/0000-0002-8458-5047>  
 A. de la Macorra  <https://orcid.org/0000-0002-1769-1640>  
 Arjun Dey  <https://orcid.org/0000-0002-4928-4003>  
 S. Gontcho A Gontcho  <https://orcid.org/0000-0003-3142-233X>  
 J. Guy  <https://orcid.org/0000-0001-9822-6793>  
 S. Juneau  <https://orcid.org/0000-0002-0000-2394>  
 T. Kisner  <https://orcid.org/0000-0003-3510-7134>  
 M. Landriau  <https://orcid.org/0000-0003-1838-8528>  
 L. Le Guillou  <https://orcid.org/0000-0001-7178-8868>  
 M. Manera  <https://orcid.org/0000-0003-4962-8934>  
 P. Martini  <https://orcid.org/0000-0002-4279-4182>  
 A. Meisner  <https://orcid.org/0000-0002-1125-7384>  
 R. Miquel  <https://orcid.org/0000-0002-6610-4836>  
 J. Moustakas  <https://orcid.org/0000-0002-2733-4559>  
 J. Nie  <https://orcid.org/0000-0001-6590-8122>  
 C. Poppett  <https://orcid.org/0000-0003-0512-5489>  
 M. Rezaie  <https://orcid.org/0000-0001-5589-7116>  
 E. Sanchez  <https://orcid.org/0000-0002-9646-8198>  
 H. Seo  <https://orcid.org/0000-0002-6588-3508>  
 G. Tarlé  <https://orcid.org/0000-0003-1704-0781>  
 H. Zou  <https://orcid.org/0000-0002-6684-3997>

## References

- Alexander, D. M., Davis, T. M., Chaussidon, E., et al. 2023, *AJ*, **165**, 124  
 Anand, A., Nelson, D., & Kauffmann, G. 2021, *MNRAS*, **504**, 65  
 Anand, A., Kauffmann, G., & Nelson, D. 2022, *MNRAS*, **513**, 3210  
 Anand, A., Guy, J., Bailey, S., et al. 2024, *AJ*, **168**, 124  
 Beckmann, R. S., Devriendt, J., Slyz, A., et al. 2017, *MNRAS*, **472**, 949  
 Benson, A. J., Bower, R. G., Frenk, C. S., et al. 2003, *ApJ*, **599**, 38  
 Best, P. N., Kauffmann, G., Heckman, T. M., et al. 2005, *MNRAS*, **362**, 25  
 Birzan, L., McNamara, B. R., Nulsen, P. E. J., Carilli, C. L., & Wise, M. W. 2008, *ApJ*, **686**, 859  
 Boehringer, H., Voges, W., Fabian, A. C., Edge, A. C., & Neumann, D. M. 1993, *MNRAS*, **264**, L25  
 Boquien, M., Burgarella, D., Roehlly, Y., et al. 2019, *A&A*, **622**, A103  
 Bower, R. G., Benson, A. J., Malbon, R., et al. 2006, *MNRAS*, **370**, 645  
 Braun, R., Bourke, T., Green, J. A., Keane, E., & Wagg, J. 2015, Proc. of Advancing Astrophysics with the Square Kilometre Array (AASKA14), 174  
 Brodzeller, A., Dawson, K., Bailey, S., et al. 2023, *AJ*, **166**, 66  
 Bruzual, G., & Charlot, S. 2003, *MNRAS*, **344**, 1000  
 Carilli, C. L., Perley, R. A., & Harris, D. E. 1994, *MNRAS*, **270**, 173  
 Chabrier, G. 2003, *PASP*, **115**, 763  
 Chaussidon, E., Yèche, C., Palanque-Delabrouille, N., et al. 2023, *ApJ*, **944**, 107  
 Chen, S.-F. S., Simcoe, R. A., Torrey, P., et al. 2017, *ApJ*, **850**, 188  
 Cherrey, M., Bouché, N., Zabl, J., et al. 2024, *MNRAS*, **528**, 481  
 Cooper, A. P., Kuposov, S. E., Allende Prieto, C., et al. 2023, *ApJ*, **947**, 37  
 Cowie, L. L., & Binney, J. 1977, *ApJ*, **215**, 723  
 Crain, R. A., & van de Voort, F. 2023, *ARA&A*, **61**, 473  
 Croton, D. J., Springel, V., White, S. D. M., et al. 2006, *MNRAS*, **365**, 11  
 DESI Collaboration, Abareshi, B., Aguilar, J., et al. 2022, *AJ*, **164**, 207  
 DESI Collaboration, Adame, A. G., Aguilar, J., et al. 2024a, *AJ*, **167**, 62  
 DESI Collaboration, Adame, A. G., Aguilar, J., et al. 2024b, *AJ*, **168**, 58  
 DESI Collaboration, Adame, A. G., Aguilar, J., et al. 2024c, arXiv:2404.03000  
 DESI Collaboration, Adame, A. G., Aguilar, J., et al. 2024d, arXiv:2404.03001  
 DESI Collaboration, Adame, A. G., Aguilar, J., et al. 2024e, arXiv:2404.03002  
 DESI Collaboration, Aghamousa, A., Aguilar, J., et al. 2016a, arXiv:1611.00036  
 DESI Collaboration, Aghamousa, A., Aguilar, J., et al. 2016b, arXiv:1611.00037  
 Davé, R., Finlator, K., & Oppenheimer, B. D. 2012, *MNRAS*, **421**, 98  
 Davé, R., Anglés-Alcázar, D., Narayanan, D., et al. 2019, *MNRAS*, **486**, 2827  
 Dey, A., Schlegel, D. J., Lang, D., et al. 2019, *AJ*, **157**, 168  
 Di Francesco, J., Chalmers, D., Denman, N., et al. 2019, *Canadian Long Range Plan for Astronomy and Astrophysics White Papers*, 2020, 32  
 Donahue, M., & Voit, G. M. 2022, *PhR*, **973**, 1  
 Eckert, D., Gaspari, M., Gastaldello, F., Le Brun, A. M. C., & O'Sullivan, E. 2021, *Univ.*, **7**, 142  
 Elahi, P. J., Power, C., Lagos, C. d. P., Poulton, R., & Robotham, A. S. G. 2018, *MNRAS*, **477**, 616  
 Fabian, A. C. 2012, *ARA&A*, **50**, 455  
 Fabian, A. C., & Nulsen, P. E. J. 1977, *MNRAS*, **180**, 479  
 Fabian, A. C., Sanders, J. S., Allen, S. W., et al. 2003, *MNRAS*, **344**, L43  
 Fasano, G., & Franceschini, A. 1987, *MNRAS*, **225**, 155  
 Gabor, J. M., Davé, R., Oppenheimer, B. D., & Finlator, K. 2011, *MNRAS*, **417**, 2676  
 Gehrels, N. 1986, *ApJ*, **303**, 336  
 Girelli, G., Pozzetti, L., Bolzonella, M., et al. 2020, *A&A*, **634**, A135  
 Gitti, M., Brighenti, F., & McNamara, B. R. 2012, *AdAst*, **2012**, 950641  
 Gordon, Y. A., Boyce, M. M., O'Dea, C. P., et al. 2021, *ApJS*, **255**, 30  
 Guy, J., Bailey, S., Kremin, A., et al. 2023, *AJ*, **165**, 144  
 Hafen, Z., Faucher-Giguère, C.-A., Anglés-Alcázar, D., et al. 2019, *MNRAS*, **488**, 1248  
 Hahn, C., Wilson, M. J., Ruiz-Macias, O., et al. 2023, *AJ*, **165**, 253  
 Hardcastle, M. J., & Croston, J. H. 2020, *NewAR*, **88**, 101539  
 Hardcastle, M. J., Williams, W. L., Best, P. N., et al. 2019, *A&A*, **622**, A12  
 Hardcastle, M. J., Horton, M. A., Williams, W. L., et al. 2023, *A&A*, **678**, A151  
 Heckman, T. M., & Best, P. N. 2014, *ARA&A*, **52**, 589  
 Hirschmann, M., Dolag, K., Saro, A., et al. 2014, *MNRAS*, **442**, 2304  
 Hlavacek-Larrondo, J., Fabian, A. C., Edge, A. C., et al. 2012, *MNRAS*, **421**, 1360  
 Huang, Y.-H., Chen, H.-W., Sheckman, S. A., et al. 2021, *MNRAS*, **502**, 4743  
 Huang, Y.-H., Chen, H.-W., Johnson, S. D., & Weiner, B. J. 2016, *MNRAS*, **455**, 1713  
 Jarvis, M. J., & McLure, R. J. 2002, *MNRAS*, **336**, L38  
 Juneau, S., Canning, R., Alexander, D. M., et al. 2024, arXiv:2404.03621  
 Kauffmann, G., Nelson, D., Ménard, B., & Zhu, G. 2017, *MNRAS*, **468**, 3737  
 Kelly, B. C. 2007, *ApJ*, **665**, 1489  
 Kereš, D., Katz, N., Fardal, M., Davé, R., & Weinberg, D. H. 2009, *MNRAS*, **395**, 160  
 Khraykin, I. S., Sorini, D., Lee, K.-G., & Davé, R. 2024, *MNRAS*, **529**, 537  
 Kondapally, R., Best, P. N., Raouf, M., et al. 2023, *MNRAS*, **523**, 5292  
 Lacy, M., Baum, S. A., Chandler, C. J., et al. 2020, *PASP*, **132**, 035001  
 Lan, T.-W. 2020, *ApJ*, **897**, 97  
 Lan, T.-W., & Fukugita, M. 2017, *ApJ*, **850**, 156  
 Lan, T.-W., & Mo, H. 2018, *ApJ*, **866**, 36  
 Lan, T.-W., & Mo, H. 2019, *MNRAS*, **486**, 608  
 Lan, T.-W., & Prochaska, J. X. 2021, *MNRAS*, **502**, 5104  
 Lan, T.-W., Ménard, B., & Zhu, G. 2014, *ApJ*, **795**, 31  
 Lan, T.-W., Tojeiro, R., Armengaud, E., et al. 2023, *ApJ*, **943**, 68  
 Lanzetta, K. M., Turnshek, D. A., & Wolfe, A. M. 1987, *ApJ*, **322**, 739  
 Lee, D., & Seung, S. 1999, *Natur*, **401**, 788  
 McNamara, B. R., & Nulsen, P. E. J. 2007, *ARA&A*, **45**, 117  
 McNamara, B. R., & Nulsen, P. E. J. 2012, *NJPh*, **14**, 055023  
 McNamara, B. R., Nulsen, P. E. J., Wise, M. W., et al. 2005, *Natur*, **433**, 45  
 Mitchell, P. D., Schaye, J., Bower, R. G., & Crain, R. A. 2020, *MNRAS*, **494**, 3971  
 Myers, A. D., Moustakas, J., Bailey, S., et al. 2023, *AJ*, **165**, 50  
 Napolitano, L., Pandey, A., Myers, A. D., et al. 2023, *AJ*, **166**, 99  
 Nelson, D., Pillepich, A., Springel, V., et al. 2019, *MNRAS*, **490**, 3234  
 Nelson, D., Sharma, P., Pillepich, A., et al. 2020, *MNRAS*, **498**, 2391  
 Nestor, D. B., Turnshek, D. A., & Rao, S. M. 2005, *ApJ*, **628**, 637  
 Netzer, H. 2015, *ARA&A*, **53**, 365  
 Nielsen, N. M., Churchill, C. W., Kacprzak, G. G., & Murphy, M. T. 2013, *ApJ*, **776**, 114  
 Nulsen, P. E. J., Jones, C., Forman, W. R., et al. 2007, in Heating versus Cooling in Galaxies and Clusters of Galaxies, ed. H. Böhringer et al. (Berlin: Springer), 210  
 Padovani, P., Alexander, D. M., Assef, R. J., et al. 2017, *A&ARv*, **25**, 2  
 Pandge, M. B., Sonkamble, S. S., Parekh, V., et al. 2019, *ApJ*, **870**, 62  
 Peacock, J. A. 1983, *MNRAS*, **202**, 615  
 Pushkarev, A. B., Kovalev, Y. Y., Lister, M. L., & Savolainen, T. 2017, *MNRAS*, **468**, 4992  
 Rafferty, D. A., McNamara, B. R., Nulsen, P. E. J., & Wise, M. W. 2006, *ApJ*, **652**, 216  
 Raghunathan, S., Clowes, R. G., Campusano, L. E., et al. 2016, *MNRAS*, **463**, 2640

- Raichoor, A., Moustakas, J., Newman, J. A., et al. 2023, *AJ*, 165, 126
- Ramírez-Pérez, C., Pérez-Ràfols, I., Font-Ribera, A., et al. 2024, *MNRAS*, 528, 6666
- Rosario, D. J., Fawcett, V. A., Klindt, L., et al. 2020, *MNRAS*, 494, 3061
- Schlafly, E. F., Kirkby, D., Schlegel, D. J., et al. 2023, *AJ*, 166, 259
- Shimwell, T. W., Röttgering, H. J. A., Best, P. N., et al. 2017, *A&A*, 598, A104
- Shimwell, T. W., Hardcastle, M. J., Tasse, C., et al. 2022, *A&A*, 659, A1
- Silber, J. H., Fagrelus, P., Fanning, K., et al. 2023, *AJ*, 165, 9
- Smailagić, M., Prochaska, J. X., Burchett, J., & Zhu, G. 2023, *ApJ*, 957, 91
- Tumlinson, J., Peebles, M. S., & Werk, J. K. 2017, *ARA&A*, 55, 389
- Turner, R. J., & Shabala, S. S. 2015, *ApJ*, 806, 59
- Urry, C. M., & Padovani, P. 1995, *PASP*, 107, 803
- van Haarlem, M. P., Wise, M. W., Gunst, A. W., et al. 2013, *A&A*, 556, A2
- Voit, G. M., Bryan, G. L., Prasad, D., et al. 2020, *ApJ*, 899, 70
- Yuan, S., Zhang, H., Ross, A. J., et al. 2024, *MNRAS*, 530, 947
- Zhou, R., Dey, B., Newman, J. A., et al. 2023, *AJ*, 165, 58
- Zhu, G. 2016, arXiv:1612.06037
- Zhu, G., & Ménard, B. 2013a, *ApJ*, 770, 130
- Zhu, G., & Ménard, B. 2013b, *ApJ*, 773, 16
- Zhu, G., Ménard, B., Bizyaev, D., et al. 2014, *MNRAS*, 439, 3139
- Zinger, E., Pillepich, A., Nelson, D., et al. 2020, *MNRAS*, 499, 768
- Zou, S., Jiang, L., Shen, Y., et al. 2021, *ApJ*, 906, 32
- Zou, S., Jiang, L., Cai, Z., et al. 2024, *ApJ*, 960, 34